International Journal of Nanomedicine

Dovepress
Taylor & Francis Group

Open Access Full Text Article

ORIGINAL RESEARCH

Biomimetic Self-Oxygenated Immunoliposome for Cancer-Targeted Photodynamic Immunotherapy

Yucheng Tang[1–3,*], Tiantian Tang[1–3,*], Yongjiang Li[1–3], Junyong Wu[1–3], Xinyi Liu[1–3], Daxiong Xiang[1–3], Xiongbin Hu[1–3]

[1]Department of Pharmacy, The Second Xiangya Hospital, Central South University, Changsha, 410011, People's Republic of China; [2]Hunan Provincial Engineering Research Center of Translational Medicine and Innovative Drug, Changsha, 410011, People's Republic of China; [3]Institute of Clinical Pharmacy, Central South University, Changsha, 410011, People's Republic of China

*These authors contributed equally to this work

Correspondence: Xiongbin Hu, Department of Pharmacy, The Second Xiangya Hospital, Central South University, Changsha, 410011, People's Republic of China, Email huxiongbin@csu.edu.cn

Objective: Photodynamic therapy (PDT) is a promising strategy with significant clinical application potential for tumor treatment. However, the tumor hypoxia and limited efficacy against tumor metastasis present significant limitations in the clinical application of PDT. To alleviate tumor hypoxia for PDT against tumor growth and metastasis, we developed a self-oxygenated immunoliposome by encapsulating the catalase (CAT) within the liposome cavity and loading the photosensitizer chlorin e6 (Ce6) and immunoadjuvant MPLA in the lipid bilayer of the immunoliposome (CAT@LP-Ce6-A). Subsequently, we fused it with the cancer cell membrane (CCM) to create the hybrid immunoliposome (CAT@LP-CCM-Ce6-A). The in vitro and in vivo anti-cancer efficacy of CAT@LP-CCM-Ce6-A-based photodynamic immunotherapy (PDIT) was evaluated.

Methods: CAT@LP-CCM-Ce6-A were characterized by size, zeta potential, transmission electron microscopy (TEM), Coomassie bright blue staining, UV spectrophotometer, and standard Goth's method. Cellular uptake, cell viability, reactive oxygen species ($^1O_2$) generation, calreticulin exposure, and ability to promote BMDCs maturation of CAT@LP-CCM-Ce6-A were evaluated in vitro. Biodistribution, anti-cancer therapeutic efficacy, and in vivo safety of CAT@LP-CCM-Ce6-A were investigated in orthotopic triple-negative breast cancer (TNBC) lung metastasis mouse models.

Results: CAT@LP-CCM-Ce6-A was successfully developed via the thin film hydration and co-extrusion method. The loading capacity of Ce6 and CAT was 4.7 ± 0.9% and 8.5 ± 0.9% respectively. CAT@LP-CCM-Ce6-A exhibited improved cellular uptake efficiency and cytotoxicity under laser irradiation against TNBC. Furthermore, CAT@LP-CCM-Ce6-A possessed enhanced anti-enzymatic degradation ability and promotion of DC maturation. In TNBC-bearing mice, CAT@LP-CCM-Ce6-A-based PDIT demonstrated remarkable therapeutic effect and antitumor immunity while maintaining minimal systemic toxicity.

Conclusion: CAT@LP-CCM-Ce6-A could be employed as an innovative approach for self-oxygenated photodynamic immunotherapy against cancer.

Keywords: liposome, photodynamic therapy, cancer, biomimetic

Introduction

Tumor metastasis is currently a major challenge in the oncological clinical practice, with approximately 90% or more cancer-related fatalities resulting from tumor metastasis.[1] Surgery, chemotherapy, and radiotherapy are the main approaches in the clinical management of malignant tumors. However, these interventions exhibit significant drawbacks, such as high toxicity, adverse effects, immunosuppression, and limited effectiveness in suppressing metastasis.[2] An optimal therapeutic strategy should effectively and safely eliminate primary tumors and inhibit tumor metastasis.

Photodynamic therapy (PDT) has emerged as a prominent strategy in cancer management for its non-invasive and spatiotemporally controllable features.[3] Compared to other conventional treatments, PDT exhibits a variety of prominent advantages, including superior safety, promising effectiveness, minimal side effects, and high repeatability.[4] During PDT

Received: 26 November 2024
Accepted: 26 February 2025
Published: 6 March 2025

implementation, photosensitizers can be activated by laser with a specific wavelength in the presence of oxygen to generate reactive oxygen species (ROS), which then induce cell death by destroying the structure and function of surrounding organelles.[5,6] Accumulating evidence highlights that PDT typically activates anti-tumor immunity. Immunogenic cell death (ICD) is defined as a cell death process capable of eliciting an immune response that enhances the therapeutic effects of PDT.[7–9] Tumor-associated antigens originating from tumor cell debris are released and captured by antigen-presenting cells (APCs) during this process, leading to the subsequent activation of $CD8^+$ T cells.[10] In addition, this process increases the exposure of calreticulin (CRT) and damage-associated molecular patterns (DAMPs) which stimulate the APCs maturation,[11,12] subsequently enhancing the immune responses.

However, both tumor eradication and ICD induction of PDT are significantly hindered by tumor hypoxia.[13–16] Studies have shown that the oxygen level in solid tumors is substantially lower than that in normal tissues.[17,18] Rapid tumor proliferation and insufficient blood flow due to an immature vascular system contribute to tumor hypoxia, leading to certain tumor regions experiencing deficient oxygen levels and severely impeding ROS generation.[17] More importantly, tumor hypoxia contributes to developing an immunosuppressive tumor microenvironment (TME).[16,18–20] Hypoxic TME can directly induce tumor-associated macrophages (TAM) to polarize towards the tumor-promoting M2 phenotype, thereby limiting the efficacy of immunotherapy by suppressing immune cell function.[21,22] Developing novel and effective strategies to alleviate tumor hypoxia is crucial for enhancing the effectiveness of PDT in inhibiting both tumor growth and metastasis.

Furthermore, studies have shown that PDT is far from being regarded as an effective strategy for preventing tumor metastasis, primarily due to the limited efficacy of the immune response.[23] To boost immune responses, PDT must be combined with other therapeutic approaches to obtain synergistic effects Existing literature highlights the benefits of combining PDT with immunotherapy. Wen et al[24] developed a PpIX-1MT nanoparticle by combining the photosensitizer PpIX with the immune checkpoint blocker 1MT. This combination therapy effectively suppressed in situ tumors and significantly inhibited tumor metastasis, demonstrating the remarkable potential of photodynamic immunotherapy (PDIT) in cancer management.

To alleviate the tumor hypoxia and enhance antitumor immunity during PDT, we developed a biomimetic self-oxygenated immunoliposome (CAT@LP-CCM-Ce6-A) to implement photodynamic immunotherapy (PDIT). The catalase (CAT), which could catalyze H_2O_2 to produce oxygen,[25] was loaded in the inner lumen of the immunoliposome. The chlorin e6 (Ce6), an FDA-approved second-generation photosensitizer,[26–28] and the immunoadjuvant monophosphoryl lipid A (MPLA),[29] a carbohydrate-based adjuvant that activates TLR4, were encapsulated in the lipid membrane of the immunoliposome. Murine breast cancer cell membranes (CCM) are hybridized into the immunoliposomal membrane to confer biomimetic and targeting features[30] (Figure 1). CAT@LP-CCM-Ce6-A can effectively accumulate at the tumor through the homologous targeting of CCM.[31] Under laser irradiation, ROS generated by Ce6 directly induces the death of tumor cells. CAT released from CAT@LP-CCM-Ce6-A produces oxygen by H_2O_2 catalyzation at the tumor site, improving tumor hypoxia. Meanwhile, CAT@LP-CCM-Ce6-A triggers strong immune responses under laser irradiation through the co-delivered immune adjuvant MPLA and inducing tumor cell ICD.

We generated an orthotopic allograft triple-negative breast cancer (TNBC) lung metastasis mouse model to evaluate the therapeutic effect of CAT@LP-CCM-Ce6-A-based PDIT. The therapeutic effect of CAT@LP-CCM-Ce6-A-based PDIT on hypoxic tumors was investigated systematically at cellular and animal levels. All findings confirm that CAT@LP-CCM-Ce6 -A-based PDIT provides an effective strategy for alleviating tumor hypoxia and inhibiting metastasis for cancer management.

Methods and Materials

Cell Culture

The murine 4T1 breast cancer cells were obtained from the Chinese Academy of Sciences Cell Bank and were maintained in RPMI-1640 (Gibco, Grand Island, NY, USA) medium supplemented with 10% fetal bovine serum (FBS) (ExCell Bio, Shanghai, China) and 1% penicillin/streptomycin (Gibco, Grand Island, NY, USA) at 37 °C with 5% CO_2.

Cell Membrane Extraction

The 4T1 membrane was prepared using a hypotonic swelling and ultrasonication method. Briefly, 4T1 cells were collected and washed three times with phosphate-buffered saline (PBS) solution. The harvested cells were then resuspended in a hypotonic

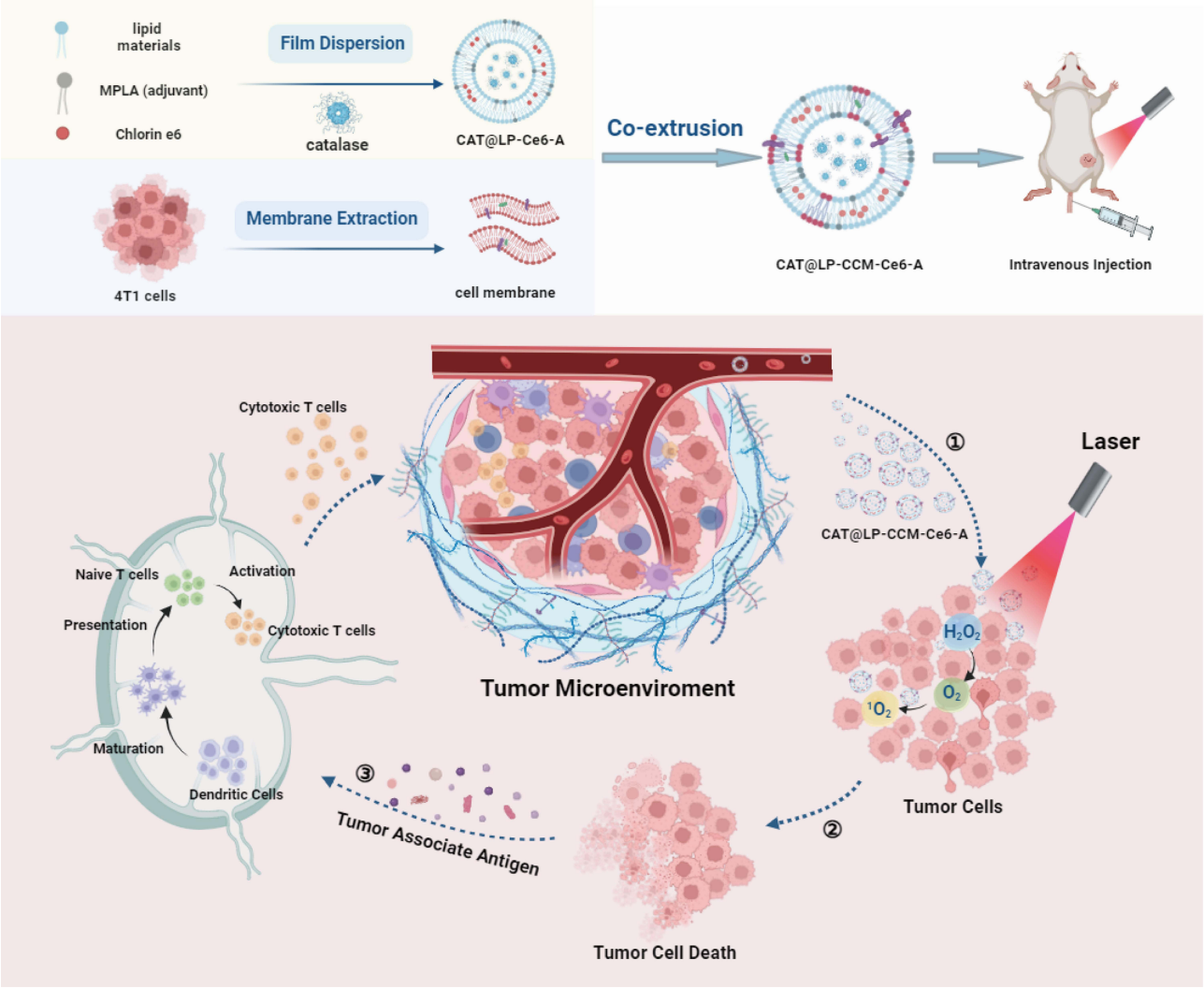

Figure 1 Schematic illustration of the preparation and application of CAT@LP-CCM-Ce6-A for the treatment of triple-negative breast cancer (TNBC) with lung metastasis in mice. This was created with BioRender.

buffer (10 mm Tris-HCl, 10 mm $MgCl_2$, and protease inhibitor without EDTA) for 1 h at 4°C. Ultrasonic crushing was then performed using an ultrasonic cell crushing machine (92-IIDN, Shanghai Aiang Instrument Co., LTD, Shanghai, China) (90 w, 20s on / 30s off) on ice for 16 min. The mixture was subsequently centrifuged at 10000 rpm at 4°C for 10 min to remove the nuclei and cytoplasm. The supernatant was subjected to ultracentrifugation at 100,000 g at 4°C for 1 h, to obtain the cancer cell membrane (CCM). The extracted cell membrane was then resuspended in PBS and stored at −80°C for further use.

Preparation of CAT@LP-CCM-Ce6-A

CAT@LP-CCM-Ce6-A was prepared by the thin film hydration technique followed by the membrane extrusion method. In brief, DPPC (Avanti Polar Lipids, USA), DSPC (Avanti Polar Lipids, USA), cholesterol (Sigma-Aldrich, USA), MPLA (Avanti Polar Lipids, USA), and Ce6 (J&K Scientific, China) were dissolved in chloroform at the following masses: 18: 4: 3.8: 1: 1, respectively. The solution was then evaporated at 30°C to form a thin film. The dried film was hydrated in 1 mL PBS containing 1mg CAT for 10 min. For the construction of CAT@LP-CCM-Ce6-A, CCM containing 100 μg membrane protein was added to the mixture. Then the mixture was subjected to a freeze-thaw cycle between 0 and 40°C for a total of 5 cycles (5 min/cycle), after which it was extruded through 100 nm polycarbonate membrane filters (Whatman) using a mini-extruder (Avanti Polar Lipids). The unbound CAT and Ce6 were removed by dialysis

https://doi.org/10.2147/IJN.S508696

method using a cellulose tubular membrane with a molecular weight cut-off of 1000 kDa (Millipore). CAT@LP-Ce6-A was prepared according to the same method without the addition of CCM.

Characterization of CAT@LP-CCM-Ce6-A

The size distribution and zeta potential of CAT@LP-Ce6-A and CAT@LP-CCM-Ce6-A were measured and compared by dynamic light scattering (DLS) (Zetasizer Nano ZS90, Malvern, UK). The morphology of CAT@LP-Ce6-A and CAT@LP-CCM-Ce6-A were obtained by transmission electron microscopy (TEM). The CAT@LP-Ce6-A and CAT@LP-CCM-Ce6-A were applied to carbon film-coated copper grids and stained with 2% phosphotungstic acid. Images were captured using a Tecnai G2 Spirit TWIN Electron Microscope (FEI, Holland). The protein profile of CAT@LP-CCM-Ce6-A was determined by sodium dodecyl sulfate-polyacrylamide gel electrophoresis (SDS-PAGE). Protein signals were detected and analyzed using a gel imaging system (ChemiDocTM Touch, Bio-Rad, USA). The storage stability of CAT@LP-CCM-Ce6-A was evaluated by monitoring the particle size in PBS and PBS containing 10% FBS at 4°C for 7 days.

Drug Loading and Release Profile

The UV absorption spectrum of Ce6 was confirmed by a UV spectrophotometer (BlueStar A, LabTech, China). Typically, the standard absorption curve of Ce6 in methanol at series concentrations was first obtained, and its linear relationship was calculated. The loading capacity of Ce6 was determined by the UV absorbance of CAT@LP-CCM-Ce6-A at 660 nm. The in vitro drug release study was conducted in PBS containing 10% FBS at different pH (7.4 and 5.5).[32] In brief, the release of CAT and Ce6 from CAT@LP-CCM-Ce6-A was measured using an ultrafiltration tube with a 1000 kDa cutoff (Millipore) against PBS containing 10% FBS at 37°C. Following a 48-hour incubation period, the concentration of the released Ce6 was quantified by the Uy, and the released CAT was quantified by enzyme labeling (TECAN) after the CAT was labeled with the fluorescent dye Cy5.5. The amount of CAT was determined by measuring the fluorescence intensity of Cy5.5.

Measurement of Catalytic Ability

The catalytic activities of the prepared nano-formulations were detected by standard Goth's method.[25] Briefly, 0.1 mL of free CAT, CAT@LP-Ce6-A, and CAT@LP-CCM-Ce6-A were added to 1 mL of a 50 mm H_2O_2 and reacted for 1 min at 37°C. Subsequently, the catalytic reaction was terminated by the addition of 1 mL ammonium molybdate (32.5 mm). Following a cooling period to 25 °C, the absorbance of the aforementioned solutions at 400 nm was measured using a UV-VIS spectrophotometer. The stability of free CAT and prepared nano-formulations against protease digestion was also evaluated. After digestion by protease K (0.5 mg/mL) for 0.25 h, 0.5 h, 1 h, 2 h, 4 h, and 8 h at 37 °C, the catalytic activity of each sample was quantified using the Goth's method previously described. The relative catalytic activity was calculated according to the following equation: The relative catalytic activity (%) = (absorbance of H_2O_2 with PBS - absorbance of H_2O_2 with nano-formulations) / (absorbance of H_2O_2 with PBS - absorbance of H_2O_2 with free CAT) × 100%.

Cytotoxicity of CAT@LP-CCM-Ce6-A with Irradiation

To study the cytotoxicity of CAT@LP-CCM-Ce6-A, 4T1 cells (8×10^3 cells/well) seeded in 96-well plates were incubated with Ce6, CAT@LP-Ce6-A and CAT@LP-CCM-Ce6-A at various concentrations (Ce6 concentration: 0 μg/mL, 0.2 μg/mL, 0.5 μg/mL, 1.0 μg/mL, 2.0 μg/mL, 5.0 μg/mL) for 2 h. The 4T1 cells were then irradiated (100 mW/cm^2, 660 nm) for 2 min and incubated for 24 h. To assess the safety of CAT@LP-CCM-Ce6-A, the cytotoxicity of the nano-formulation without laser irradiation was investigated. The phototoxicity of CAT@LP-CCM-Ce6-A under laser irradiation was also investigated to better mimic the hypoxic tumor microenvironment.[33] For hypoxia, cells were cultured in an incubation environment of 94% N_2, 1% O_2 and 5% CO_2.[34] The cell viability was assessed by the CCK-8 assay (NCM Biotech, Suzhou, China) by measuring the absorbance at 450 nm using a Multiskan FC (Thermo Fisher Scientific, USA). Statistical analysis of data was obtained from triplicate samples.

Cellular Uptake

A fluorescence co-localization experiment was conducted to evaluate the in vitro affinity of CAT@LP-CCM-Ce6-A to 4T1 cells. Briefly, 4T1 cells were evenly planted on a 24-well cell culture plate (NEST Biotechnology) at a density of 1×10^4 cells per well. CAT@LP-Ce6-A and CAT@LP-CCM-Ce6-A (Ce6 concentration: 5 μg/mL) were added to incubate 4T1 cells for 2 h. Cellular internalization was observed under an Olympus IX73 fluorescence microscope (Olympus, Japan). Meanwhile, we investigated the cellular uptake efficiency of CAT@LP-CCM-Ce6-A by CT26 cells. The ImageJ software was used to quantify the fluorescence intensity of cellular uptake and to perform statistical comparisons.

Reactive Oxygen Species ($^1O_2$) Generation

For the detection of reactive Oxygen Species ($^1O_2$), the Singlet Oxygen Sensor Green (SOSG) reagent from Sigma was employed. Briefly, free Ce6 and CAT@LP-CCM-Ce6-A (Ce6 concentration: 10 μg/mL) dispersed in PBS were mixed with SOSG (2.5 μM), followed by laser irradiation (100 mW/cm^2, 660 nm). CAT@LP-CCM-Ce6-A without laser irradiation was set as the control group. The relative fluorescence intensity at 530 nm of the solutions at different time points upon irradiation was quantified by a fluorescence spectrophotometer. Intracellular ROS levels were detected using a DCFH-DA assay (Sigma), based on the ROS-dependent oxidation of DCFH-DA to DCF. 4T1 cells were seeded at a density of 1×10^4 cells per well in a 24-well cell culture plate. Subsequently, 200 μL of CAT@LP-CCM-Ce6-A (Ce6 concentration: 5 μg/mL) was added to the cells and incubated for 2 h. The culture medium was then removed and the cells were washed 3 times with PBS. A further 200 μL DCFH-DA (20 μM) was added to the cells to estimate the level of ROS. The cell nuclei were stained by incubating the cells with 200 μL of DAPI (1 μM) for 20 min. The intracellular ROS level was then observed under a fluorescence microscope.

Calreticulin Exposure Detection

Fluorescence microscopy was employed to analyze the exposure of calreticulin (CRT) in tumor cells. The 4T1 cells were incubated with PBS, free Ce6, CAT@LP-Ce6 and CAT@LP-CCM-Ce6 (Ce6 concentration: 5 μg/mL) for 2 h before laser irradiation (2 min, 100 mW/cm^2, 660 nm). Subsequently, the cells were fixed with 4% paraformaldehyde for 30 min and then incubated with anti-CRT antibody (primary antibody) for 2 h. Following this, the cells were washed with PBS solution and a secondary antibody was added to incubate the cells at room temperature for 1 h. The calreticulin exposure on 4T1 cells was observed by fluorescence microscope and qualified by flow cytometry (FCM).

In vitro Antigen Cross-Presentation Tests and BMDCs Maturation

The maturation of dendritic cells (DCs) was evaluated by flow cytometry. Mouse bone marrow-derived DCs (BMDCs) were isolated from the femurs and tibias of 6–8 week old BALB/c mice. 4T1 cells were seeded in 24-well plates and cultured for 12 h. The medium was then replaced by RPMI 1640 with samples (PBS, Ce6, CAT@LP-Ce6-A, CAT@LP-CCM-Ce6-A, BSA@LP-CCM-Ce6-A, and CAT@LP-CCM-Ce6-A), with an equal dose of Ce6 (5 μg/mL) and co-incubated for 2 h. The cells were irradiated with a 660 nm laser for 2 min (100 mW/cm^2) and incubated for 12 h to release immunogenic substances such as DAMPs. The medium supernatant of the different groups was harvested by centrifugation (2500 rpm, 10 min) and added to co-incubate BMDCs for 48 h. LPS (400 ng/mL) was added to BMDCs as the positive control. BMDCs were then collected with centrifugation (1200 rpm, 5 min) and washed with PBS containing 10% FBS. The BMDCs were stained with FITC-CD80 and APC-CD86 for 15 min and analyzed by FCM.

Animal Models

Female BALB/c mice (6–8 weeks) were purchased from Slake Jingda Experimental Animal Co., LTD (Hunan, China) and maintained in specific pathogen-free (SPF) faculties. The animal experiments were approved by the Department of Laboratory Animals of Central South University (Approval No. 2021455) and all animals were treated following the Institutional Animal Care and Use Committee (IACUC) approved procedures. The orthotopic TNBC mouse model was generated subcutaneously by implanting 1×10^6 4T1 cells (in 100 μL PBS) into the mouse's fourth right mammary fat pad. The in situ TNBC mouse model was established in 5–7 days. For the establishment of TNBC lung metastasis mouse model, 2×10^5 4T1 cells (in 50 μL PBS) were further administered intravenously via tail vein infusion in the orthotopic TNBC mouse model.

Biodistribution of CAT@LP-CCM-Ce6-A

The biodistribution of CAT@LP-CCM-Ce6-A was evaluated in the orthotopic TNBC lung metastasis mouse model. Once the tumor volume reached approximately 200 mm^3, the mice were randomly divided into three groups with the different treatments of free Ce6, CAT@LP-Ce6-A, and CAT@LP-CCM-Ce6-A, with an equal dose of Ce6 (2.5 mg/kg) administered via tail vein injection, respectively. The fluorescence signal of Ce6 at the tumor site was monitored at 4 h, 8 h, 12 h, and 24 h post-injection using the in vivo imaging system AniView100 (Biolight Biotechnology Co., LTD, China). The mice were sacrificed after 24 h post-injection to capture the fluorescence images of major organs and the excised tumors. Subsequently, the fluorescence intensity of region-of-interests (ROI) was analyzed using the Living Image Software.

Tumor Hypoxia Identification

The hypoxia probe pimonidazole was employed to ascertain the oxygen level within tumors in the orthotopic TNBC lung metastasis mouse model. When the tumor volume approached 200 mm^3, PBS, BSA@LP-CCM-Ce6-A, CAT@LP-Ce6 -A, and CAT@LP-CCM-Ce6-A, each containing an equal dose of Ce6 (3.3 mg/kg), were administered via the tail vein. Following a 12-hour interval, pimonidazole (1.5 mg) was administered intraperitoneally to the mice following the manufacturer's instructions. The mice were euthanized to remove the tumors 1 h after the injection, which were then processed for frozen analysis. The tumor hypoxia was identified by fluorescence microscopy.

In vivo Antitumor Effect and Safety Profiles

TNBC lung metastasis mouse models were developed to investigate the anti-tumor effect of CAT@LP-CCM-Ce6-A. The tumor-bearing mice were injected with PBS, Ce6, CAT@LP-Ce6-A, CAT@LP-CCM-Ce6, BSA@LP-CCM-Ce6-A, and CAT@LP-CCM-Ce6-A at an equal dose of Ce6 (3.3 mg/kg) when the tumor volume reached nearly 100 mm^3. After the injection for 12 h, the mice were irradiated with a 660 nm laser (100 mW/cm^2) for 30 min. The mice were treated on days 6, 7, and 8, totaling three treatments. The tumor growth and the body weight were measured and recorded every 2 days for 24 days. The tumor volume was calculated as follows: $V = (length) \times (width)^2/2$. Then, the mice were sacrificed on day 25 to collect the tumors, lungs and lymph nodes. The pulmonary metastatic nodules were counted to detect the micro-metastatic foci, and the lungs were stained by hematoxylin and eosin (H&E) staining for histopathological analysis. Survival curves of mice were estimated using the Kaplan-Meier method.

To evaluate the in vivo safety of CAT@LP-CCM-Ce6-A, the hemolysis assay was first performed to investigate the hemolytic potential to evaluate the safety of CAT@LP-CCM-Ce6-A. The red blood cells were diluted with PBS to prepare the red blood cell suspension. The red blood cells suspended in distilled water was regarded as the positive control, and the blood cells diluted with PBS were the negative control. Different formulations (the equivalent concentration of Ce6: 5 μg/mL) were added to the red blood cell solution. These samples were incubated at 37 °C for 4 h, then observed hemolysis and measured the absorbance at 560 nm to evaluate the safety of CAT@LP-CCM-Ce6-A. Furthermore, the blood samples and major organs (including heart, liver, spleen and kidney) were collected 7 days (day 15) after the last laser irradiation, and fixed in 4% paraformaldehyde and then stained with H&E to assess potential organ damage. The serum samples were analyzed to assess liver and kidney function. The levels of related factors including aspartate aminotransferase (AST), alanine aminotransferase (ALT), urea nitrogen (BUN), and creatinine (CR) were quantified.

Flow Cytometry Analysis of Immune Activation

The release of MPLA and immunogenic substances endowed the potential capacity of CAT@LP-CCM-Ce6-A-based PDIT to trigger the immune response. Therefore, the immune cell infiltration and activation were evaluated by flow cytometry. The tumor-draining lymph nodes (TDLNs) and tumors of the mice were collected 7 days (day 15) after the last laser irradiation to analyze immune activation. Samples were placed in six-well plates (NEST, China) containing Dulbecco's phosphate-buffered saline (DPBS) with 5% fetal bovine serum. The samples were gently disrupted, washed twice with buffer, and filtered through a 70 μm cell strainer (Biosharp, China) to obtain single-cell suspensions. Red blood cells were lysed using the lysis buffer. Following this, the cells were pelleted by centrifugation at 300 g for 5 min and resuspended at 1×10^6 cells/mL. For the identification of DCs, cells obtained from TDLNs were stained with antibodies against the following markers: PE-CD11c, FITC-CD80 and APC-CD86. For the detection of T cells, cells

were incubated with PE-CD3, APC-CD8 and FITC-CD4. Furthermore, cells obtained from tumors were stained with FITC-CD11b, PE-F4/80 and APC-CD206 to determine the percentage of M2 macrophages in tumors. All the staining procedures were conducted following the manufacturer's protocols. Following staining, cells were washed twice and analyzed by flow cytometry.

Statistics Analysis

Data were presented as means ± Standard deviation (SD) for the control and experimental samples. GraphPad Prism 8 was used to plot and compare the data. A two-tailed Student's *t*-test was performed at the significance level of $\alpha = 0.05$ to evaluate differences between the two groups. One-way analysis of variance (ANOVA) was performed to test the statistical significance of difference among three or more groups. The number of replicates is indicated in the legend of each figure The statistical significance was set at * $P < 0.05$, ** $P < 0.01$ and *** $P < 0.001$.

Results and Discussions

Preparation and Characterization of CAT@LP-CCM-Ce6-A

CAT@LP-Ce6-A and CAT@LP-CCM-Ce6-A were formulated via thin film hydration and subsequent extrusion through a 100 nm polycarbonate membrane. Compared to CAT@LP-Ce6-A (mode size: 139.33 ± 2.52 nm, PDI: 0.083 ± 0.021), the hydrated size of CAT@LP-CCM-Ce6-A (mode size: 161.33 ± 3.51 nm, PDI: 0.095 ± 0.032) was marginally larger, yet remained within a reasonable size range (Figure 2A). The zeta potential of CAT@LP-CCM-Ce6-A was - 26.7 ± 2.5 mV, which was lower than that of CAT@LP-Ce6-A (−18.7 ± 1.7 mV) (Figure 2B). The CCM decreased the zeta potential of CAT@LP-Ce6-A, indicating the successful fusion of CAT@LP-Ce6-A with CCM. TEM images (Figure 2C) demonstrated that CAT@LP-Ce6-A and CAT@LP-CCM-Ce6-A were both spherical with good mono-dispersity.

To confirm the successful hybridization of the immunoliposome with CCM, Coomassie blue staining was employed to characterize the protein profiles of CCM and CAT@LP-CCM-Ce6-A. As illustrated in Figure 2D, similar protein bands were displayed between CCM and CAT@LP-CCM-Ce6-A, further confirming the fusion of the liposome and cancer cell membrane (CCM) and the successful development of the hybrid liposome.[31,35] The standard absorption curve of Ce6 in methanol was also obtained at 660 nm by UV spectrophotometer. The UV absorption spectrum of free Ce6, CAT@LP-CCM-A, and CAT@LP-CCM-Ce6-A at 660 nm demonstrated that Ce6 was successfully loaded in CAT@LP-CCM-Ce6-A (Figure 2E). To further explore the applicability of CAT@LP-CCM-Ce6-A in self-oxygenated PDIT, we evaluated the drug loading capacity and encapsulation efficiency of Ce6 and CAT in CAT@LP-CCM-Ce6-A. The loading capacity of Ce6 and CAT was 4.7 ± 0.9% and 8.5 ± 0.9%, respectively, while the encapsulation efficiency of Ce6 and CAT was 69.5 ± 9.6% and 57.4 ± 9.2%. The cumulative release rate of Ce6 and CAT under pH 7.4 (in vivo neutral physiological milieu) and pH 5.5 (acidic tumor microenvironment[32]) was examined. As illustrated in Figure 2F, the 48 h cumulative release of Ce6 and CAT under pH 7.4 was 48.4 ± 8.2% and 57.4 ± 9.4%, respectively, while the 48 h cumulative release of Ce6 and CAT in an acidic environment (pH 5.5) was 65.3± 9.1% and 71.5± 11.2%. These indicated that the acidic environment can accelerate liposome rupture, leading to the release of encapsulated cargo. Therefore, the CAT@LP-CCM-Ce6-A formulation may help to protect the encapsulated drugs in the circulatory system and facilitate drug release in the acidic tumor microenvironment.

We also measured the stability of CAT@LP-CCM-Ce6-A by determining the changes in the particle size of CAT@LP-CCM-Ce6-A in PBS and 10% FBS at 4°C. As illustrated in Figure 2G, the particle size of CAT@LP-CCM-Ce6-A remained largely unchanged in PBS and 10% FBS for 7 days, demonstrating excellent storage stability and establishing a solid foundation for subsequent in vitro and in vivo evaluations.

Due to the presence of numerous proteases, CAT can be easily degraded by proteinase and rapidly deactivated of enzyme activities during circulation.[28,36] To verify the anti-enzymatic degradation ability of CAT@LP-CCM-Ce6-A, we employed Goth's method to quantitatively investigate the enzyme activities at different time intervals under the presence of proteinase K.[37] As illustrated in Figure 2H, the CAT of CAT@LP-Ce6-A and CAT@LP-CCM-Ce6-A exceeded 80% enzyme activity after incubation with proteinase K for 8 h at 37°C. The enzyme activity was strikingly higher than free CAT (20%) under the same condition, thereby confirming the protective effect of liposomes on preventing CAT from

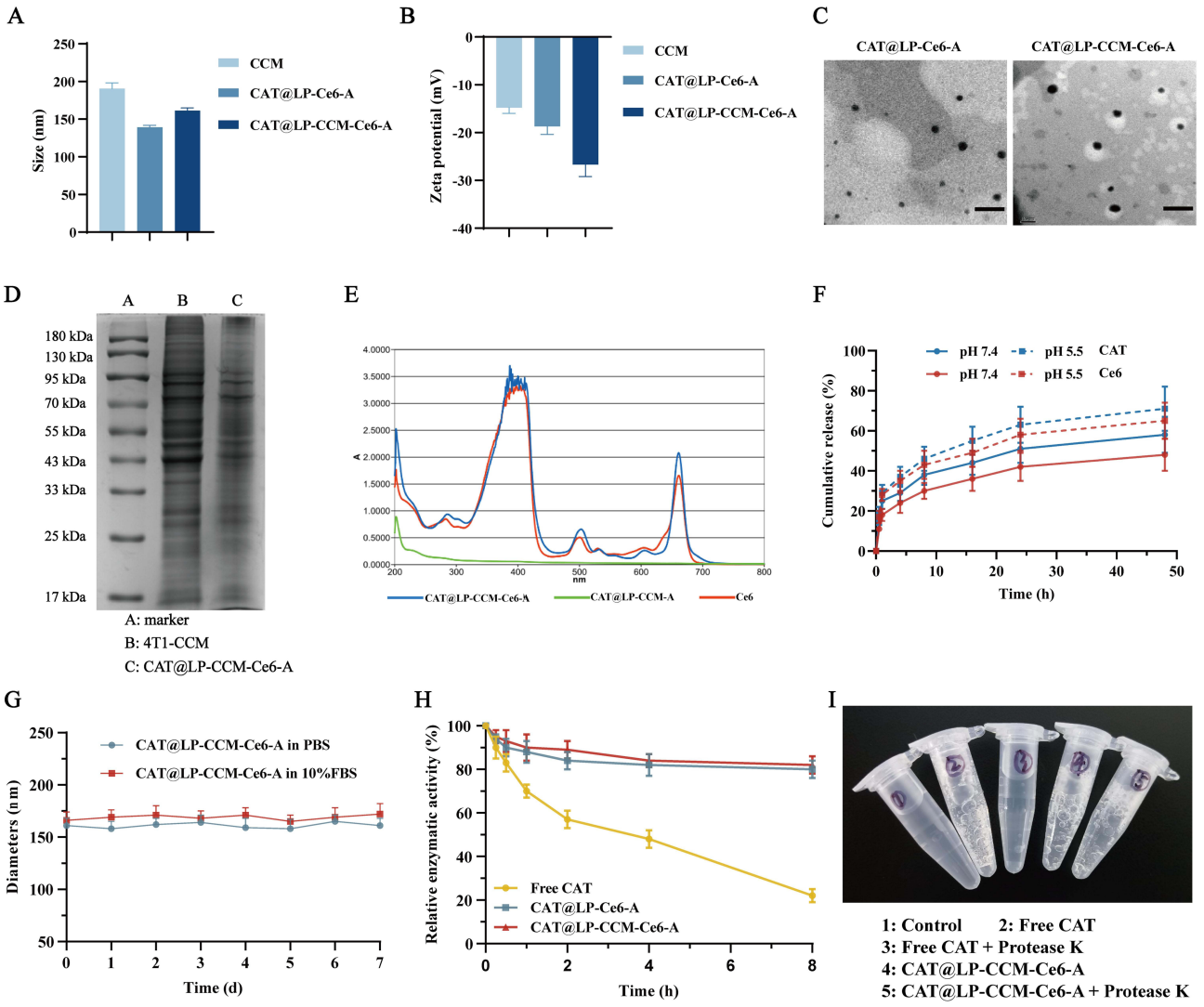

Figure 2 Characterization and enzymatic activity of CAT@LP-CCM-Ce6-A. (**A**) Particle size distribution and (**B**) zeta potential measured by dynamic light scattering (DLS). (**C**) TEM images of CAT@LP-Ce6-A and CAT@LP-CCM-Ce6-A, scale bar = 200 nm. (**D**) Coomassie blue staining analysis of 4T1 cell membrane (CCM) and CAT@LP-CCM-Ce6-A. (**E**) UV-vis absorption spectrum of free Ce6, CAT@LP-CCM-A and CAT@LP-CCM-Ce6-A. (**F**) In vitro cumulative release of CAT and Ce6 from CAT@LP-CCM-Ce6-A under physiological (pH 7.4) and acidic (pH 5.5) conditions as 37 °C. (**G**) Storage stability of CAT@LP-CCM-Ce6-A in PBS and 10% FBS. (**H**) The relative enzymatic activity of free CAT, CAT@LP-Ce6-A, and CAT@LP-CCM-Ce6-A after protease K digestion at different time. (**I**) Image showing the O_2 production of free CAT and CAT@LP-CCM-Ce6-A in H_2O_2 solutions. Data are expressed as mean ± SD (n=3).

denaturing under physiological conditions. Additionally, the catalytic decomposition of H_2O_2 by CAT@LP-CCM-Ce6-A treated with proteinase K for 24 h was comparable to CAT@LP-CCM-Ce6-A group (Figure 2I). These results further demonstrated that the encapsulation of CAT in the immunoliposome effectively prevented CAT from being degraded by proteases, thereby improving the stability of CAT in the physiological environment.

Overall, CAT@LP-CCM-Ce6-A had the potential to catalyze H_2O_2 at the tumor site to generate oxygen, thereby promoting the therapeutic efficacy of PDT and reversing immunosuppressive TME.

In vitro Anticancer Effect

A fluorescence co-localization experiment was applied to investigate the cellular uptake efficiency of CAT@LP-CCM-Ce6-A. As shown in Figure 3A, the markedly elevated fluorescence intensity of CAT@LP-CCM-Ce6-A in 4T1 cells was observed, which was twice that of the free Ce6 group. This indicated that CAT@LP-CCM-Ce6-A exhibited superior affinity for 4T1 cells. Furthermore, a comparable and weak cellular uptake efficiency of CAT@LP-Ce6-A and CAT@LP-CCM-Ce6-A was observed in CT26 cells (Figure 3B and C), confirming that the CCM derived from 4T1 cells endowed

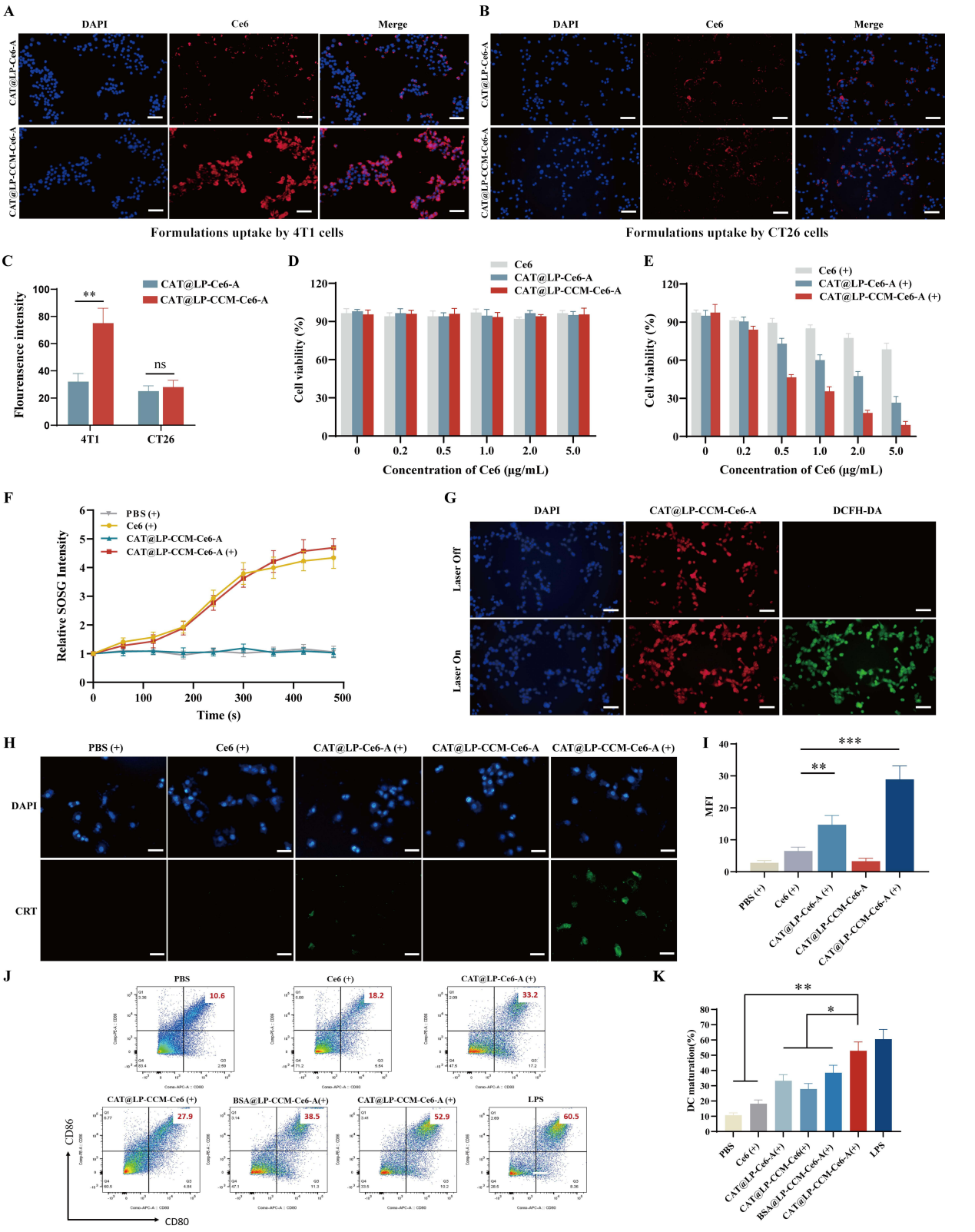

Figure 3 Cellular uptake, cytotoxicity and immune stimulation of CAT@LP-CCM-Ce6-A. (**A**) The cellular uptake of CAT@LP-Ce6-A and CAT@LP-CCM-Ce6-A by 4T1 cells and (**B**) CT26 cells, and (**C**) the analysis of the fluorescence intensity, scale bar = 200 μm. (**D**) The cell viability of 4T1 cells treated with different formulations at various concentrations without laser irradiation or (**E**) with laser irradiation, as determined by the CCK-8 assay. (**F**) Generation of $^1O_2$ in PBS, free Ce6, and CAT@LP-CCM-Ce6-A. (**G**) The intracellular ROS generation in 4T1 cells treated with CAT@LP-CCM-Ce6-A before or after laser irradiation, DCFH-DA was used to measure the intracellular ROS levels, scale bar = 200 μm. (**H**) Fluorescence images and (**I**) mean fluorescence intensity (MFI) of CRT exposed on 4T1 cells after different treatments, scale bar = 100 μm. (**J**) In vitro DCs activation in 4T1 cells treated with different formulations, and (**K**) the column statistical data. (+) refers to 660 nm laser irradiation. Data are expressed as mean ± SD (n=3). * P<0.05, ** P<0.01, *** P<0.001.

https://doi.org/10.2147/IJN.S508696

CAT@LP-CCM-Ce6-A with homologous targeting ability towards 4T1 cells. As illustrated in Figure 3D and E, no obvious cytotoxicity in the absence of laser irradiation was observed in the three treatments while pronounced cytotoxicity against 4T1 cells was observed with laser irradiation under normoxic conditions. The cell viability of the CAT@LP-CCM-Ce6-A group (9.0 ± 2.8%) was significantly lower than that of the free Ce6 (68.5 ± 4.9%) and the CAT@LP-Ce6-A group (26.5 ± 4.9%) at the Ce6 concentration of 5 μg/mL. This was likely attributed to the homophilic targeting of CAT@LP-CCM-Ce6-A, which enhanced the intracellular delivery of Ce6. To systematically evaluate the phototoxicity of CAT@LP-CCM-Ce6-A, we further investigate the cytotoxicity of CAT@LP-CCM-Ce6-A against 4T1 cells under hypoxic conditions (Figure S1). At the Ce6 concentration of 5 μg/mL, the cell viability of free Ce6, CAT@LP-Ce6-A and CAT@LP-CCM-Ce6-A group were 74.3 ± 3.9%, 32.2 ± 4.8%, and 13.5±2.2% respectively. Under hypoxic conditions, the cytotoxicity of all the three formulations was slightly weakened compared to that under normoxic conditions. This attenuation is likely attributed to the oxygen-dependent nature of the photosensitizer's activity, which is limited in the low-oxygen environments.[33] These results underscored the potential of our synergistic strategy involving the co-delivery of photosensitizer and CAT to tumors, holding high promise for overcoming hypoxia-related limitations in PDT and thereby enhancing the efficacy of PDT.

$^1O_2$ is generated by oxygen under laser irradiation with a photosensitizer, and it is a crucial indicator of the PDT. Singlet Oxygen Sensor Green (SOSG), a $^1O_2$ detection probe, was employed in this experiment for in vitro $^1O_2$ detection.[38] As illustrated in Figure 3F, the relative SOSG intensity of CAT@LP-CCM-Ce6-A in the absence of laser irradiation demonstrated no discernible change, in alignment with the PBS group, suggesting the potential safety of CAT@LP-CCM-Ce6-A. Following laser irradiation, CAT@LP-CCM-Ce6-A was observed to effectively produce $^1O_2$, with a comparable ability to produce $^1O_2$ to that of free Ce6. The elevated ROS levels in 4T1 cells conferred by CAT@LP-CCM-Ce6-A were also evaluated via the DCFH-DA assay.[39] As illustrated in Figure 3G and Figure S2, a notable green fluorescence signal was observed in 4T1 cells treated with CAT@LP-CCM-Ce6-A following laser irradiation, whereas no discernible fluorescence was observed without laser irradiation. This suggested that CAT@LP-CCM-Ce6-A could effectively produce ROS in cells with laser irradiation. These results demonstrated that laser irradiation successfully stimulated CAT@LP-CCM-Ce6-A to produce ROS in cells, thereby inducing tumor cell death.

In vitro Immune Activation

Studies have reported that PDT kills tumor cells directly and induces immunogenic cell death (ICD), activating anti-tumor immunity.[9,40] CRT exposed on the surface has been widely used as a biological marker molecule for the identification of ICD in cancer cells.[6] Herein, fluorescence microscopy was utilized to analyze CRT exposure in 4T1 cells after irradiation. As illustrated in Figure 3H and I, significant exposure of CRT (green fluorescent) was observed on the surface of 4T1 cells treated with CAT@LP-CCM-Ce6-A in comparison to PBS, Ce6, and CAT@LP-Ce6-A under laser irradiation. No fluorescent signal was detected in cells exposed to CAT@LP-CCM-Ce6-A without irradiation. These results demonstrated that CAT@LP-CCM-Ce6-A induced immunogenic cell death with laser irradiation while remaining safe under non-irradiation conditions.

Research indicates that PDT can modify the tumor microenvironment, attracting inflammatory and immune mediators that facilitate the initiation of anti-tumor immunity. DCs activation and antigen cross-presentation are pivotal in the generation of robust immune responses.[41] To further assess the immune-activating potential of CAT@LP-CCM-Ce6-A-based PDIT, an in vitro BMDCs maturation assay was conducted to investigate the immune-activating capacity of CAT@LP-CCM-Ce6 -A-based PDIT. The maturation markers CD86 and CD80 of DCs were analyzed by flow cytometry.[42] As illustrated in Figures 3J and K, the proportion of $CD80^+CD86^+$ BMDCs is significantly elevated in the CAT@LP-CCM-Ce6-A group (52.9 ± 5.8%) in comparison to PBS (10.6 ± 1.6%), Ce6 (18.2 ± 2.5%), CAT@LP-Ce6-A (33.2 ± 4.1%), CAT@LP-CCM-Ce6 (27.9 ± 3.6%) and BSA@LP-CCM-Ce6-A (38.5 ± 4.9%) under irradiation, slightly lower than that of the LPS group (60.5 ± 6.4%). These findings demonstrated that CAT@LP-CCM-Ce6-A-based photodynamic immunotherapy could effectively promote DCs maturation, thereby exhibiting significant immunotherapeutic potential to stimulate antitumor immune responses in vivo.

Tumor Targeting and Hypoxia Relief

To evaluate the in vivo tumor-targeting ability of CAT@LP-CCM-Ce6-A, different formulations (including free Ce6, CAT@LP-Ce6-A, and CAT@LP-CCM-Ce6-A) were intravenously injected into tumor-bearing mice via the tail vein at an equivalent dose of Ce6 (2.5 mg/kg). In Figure 4A, free Ce6 exhibited no accumulation at the tumor site, only a faint fluorescence signal was detected in the liver of the mice 12 h post-injection. As compared to CAT@LP-Ce6-A, mice injected with CAT@LP-CCM-Ce6-A exhibited the most pronounced fluorescence signals at 8 and 12 h, which may be attributed to the homologous targeting of CCM. These results demonstrated that CAT@LP-CCM-Ce6-A effectively addressed the challenges associated with the lack of tumor-targeting ability and the rapid clearance of Ce6. The biological distribution of free Ce6, CAT@LP-Ce6-A, and CAT@LP-CCM-Ce6-A in major organs and tumors at 24 h was shown in Figure 4B. It can also be observed that the tumor of mice exposed to CAT@LP-CCM-Ce6-A exhibited the most pronounced accumulation, with a fluorescence signal intensity 2.3 times of the CAT@LP-Ce6-A group (Figure 4C).

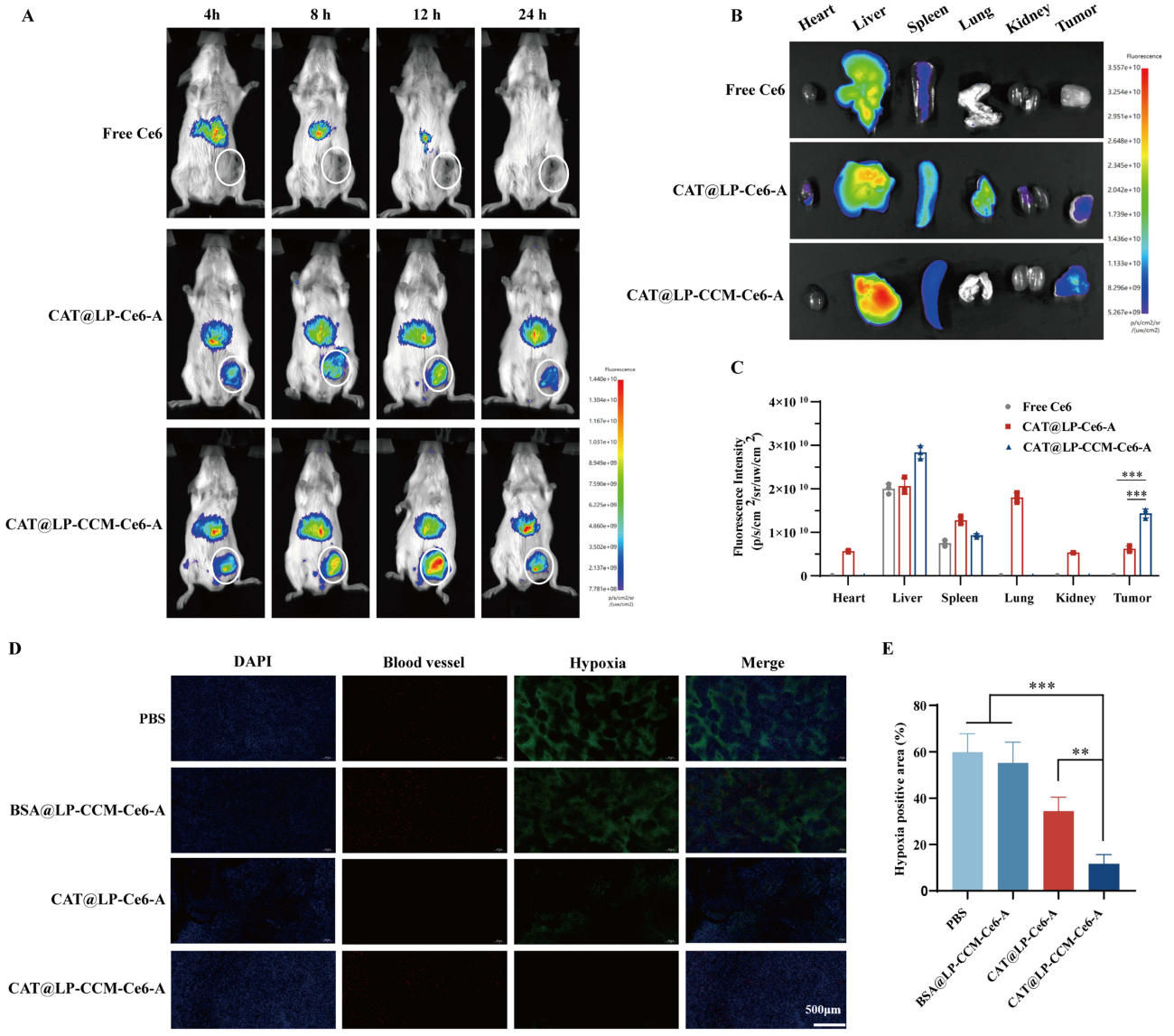

Figure 4 Tumor targeting and hypoxia relief of CAT@LP-CCM-Ce6-A. (**A**) In vivo biodistribution of free Ce6, CAT@LP-Ce6-A, and CAT@LP-CCM-Ce6-A in tumor-bearing mice assessed at 4, 8, 12, and 24 h post-injection. White circle represents the tumor region. (**B**) Ex vivo biodistribution of free Ce6, CAT@LP-Ce6-A, and CAT@LP-CCM-Ce6-A in major organs and tumors. (**C**) Quantification of fluorescence intensity in ex vivo major organs and tumors. (**D**) Immunofluorescence images of the tumors, the hypoxia areas, and blood vessels stained with anti-pimonidazole antibody (green) and anti-CD31 antibody (red), respectively. Scale bar = 500 μm. (**E**) The relative hypoxia-positive areas analyzed via the ImageJ software. Data are expressed as mean ± SD (n = 3). ** $P<0.01$, *** $P<0.001$.

https://doi.org/10.2147/IJN.S508696

The hypoxic tumor microenvironment not only greatly limits the effectiveness of PDT, but also fosters the formation of an immunosuppressive tumor microenvironment, which in turn promotes tumor invasion and metastasis. Enhancing the oxygen supply in the hypoxic environment of solid tumors is an effective strategy to enhance PDT efficacy.[43] Here, we evaluated the ability of CAT@LP-CCM-Ce6-A to reduce hypoxia in tumors using the hypoxia probe. The results demonstrated that CAT@LP-CCM-Ce6-A treatment resulted in a significant reduction in the hypoxic region (pimonidazole staining) to 11.6% ± 4.2%, in comparison to BSA@LP-CCM-Ce6-A (55.1% ± 9.4%) and CAT@LP-Ce6-A (34.4% ± 6.5%) (Figure 4D and E). These results indicated that CAT@LP-CCM-Ce6-A released CAT to catalyze endogenous H_2O_2 and produce O_2 in the tumor, thus significantly reducing tumor hypoxia.

In vivo Antitumor Efficacy

Tumor metastasis is the main cause of cancer-related morbidity and mortality. Therefore, we explored the antitumor effect and lung-metastasis inhibition of CAT@LP-CCM-Ce6-A-based PDIT in the TNBC lung metastasis mouse models (Figure 5A). When the tumor reached a volume of 100 mm^3, mice were randomly allocated into 6 groups and administered intravenous injections of PBS, Ce6, CAT@LP-Ce6-A, CAT@LP-CCM-Ce6, BSA@LP-CCM-Ce6-A and CAT@LP-CCM-Ce6-A (Ce6=3.3 mg/kg). The treatment of CAT@LP-Ce6-A, CAT@LP-CCM-Ce6, BSA@LP-CCM-Ce6-A, and CAT@LP-CCM-Ce6-A impeded tumor growth in comparison to the growth observed in the PBS and Ce6 groups (Figure 5B and E). The tumor volume and tumor weight of mice exposed to CAT@LP-CCM-Ce6-A-based PDIT exhibited the most significant decrease (Figure 5C and D), indicating the enhanced anti-tumor effect of CAT@LP-CCM-Ce6-A. Additionally, the CAT@LP-CCM-Ce6-A-based PDIT resulted in a significant prolongation of the median survival time of mice (50 days) in comparison to other treatments, including PBS (23 days), Ce6 (27 days), CAT@LP-Ce6-A (33 days), CAT@LP-CCM-Ce6 (40 days), and BSA@LP-CCM-Ce6-A (36 days) (Figure 5F).

Metastasis in vital organs of breast cancer is identified as the leading cause of breast cancer-related mortality. To evaluate the lung metastasis inhibition of CAT@LP-CCM-Ce6-A-based PDIT, the number of metastatic nodules in the lung was examined and histologically assessed by H&E staining. As illustrated in Figure 5G and H, the average number of metastatic nodules in the lungs of the mice treated with CAT@LP-CCM-Ce6-A was significantly less than that of mice treated with CAT@LP-Ce6-A, CAT@LP-CCM-Ce6, and BSA@LP-CCM-Ce6-A. In addition, the H&E staining of the lungs verified almost no metastasis in the tumor treated with CAT@LP-CCM-Ce6-A, while numerous metastatic foci were observed in the other groups (Figure 5I). These results suggested that CAT@LP-CCM-Ce6-A-based PDIT greatly inhibited the metastasis of TNBC to the lung. The significant inhibition of tumor growth, extended survival time, and suppression of tumor metastasis achieved through CAT@LP-CCM-Ce6-A-based PDIT demonstrated the enhanced antitumor ability of CAT@LP-CCM-Ce6-A. In conclusion, the CAT@LP-CCM-Ce6-A-based photodynamic therapeutic strategy demonstrated excellent treatment efficacy in the TNBC lung metastasis mouse model.

Enhanced Antitumor Immunity

The release of MPLA and immunogenic substances endowed CAT@LP-CCM-Ce6-A-based PDIT with the potential to stimulate antitumor immunity. The significant inhibition of lung metastasis in CAT@LP-CCM-Ce6-A-based PDIT inspired us to investigate antitumor immunity further. We evaluated the immune cell infiltration and activation via flow cytometry. In the tumor microenvironment, tumor-associated macrophages (TAMs) play a crucial role in tumor growth, survival, invasion, metastasis, angiogenesis, inflammation, and immunoregulatory processes.[44,45] We first investigated the TAM infiltration in the mice after different interventions. As illustrated in Figure 6A and B, the proportion of M2-polarized TAM ($CD11b^+F4/80^+CD206^+$) in the tumor was markedly diminished in the CAT@LP-CCM-Ce6-A group in comparison to the PBS and free Ce6 groups. The effect of CAT@LP-CCM-Ce6-A-based PDIT on the in vivo DCs maturation was also investigated. Consistent with the in vitro DCs maturation results, CAT@LP-CCM-Ce6-A-based PDIT markedly increased the ratio of $CD80^+CD86^+$ BMDCs (32.6% ± 5.3%) in TDLNs compared to other treatments (Figure 6C and D). This indicates that CAT@LP-CCM-Ce6-A-based PDIT potently induced DCs maturation, which was critical for eliciting robust immune responses. Additionally, we examined the infiltration of T lymphocytes in tumors. In Figure 6E, we observed that CAT@LP-CCM-Ce6-A with irradiation resulted in the most remarkable $CD4^+$ and $CD8^+$ T lymphocyte infiltration as compared with PBS, Ce6, CAT@LP-Ce6-A, CAT@LP-CCM-Ce6, and BSA@LP-CCM-Ce6-A. It is well-recognized that $CD8^+$ T cells can exert a direct anti-tumor effect.

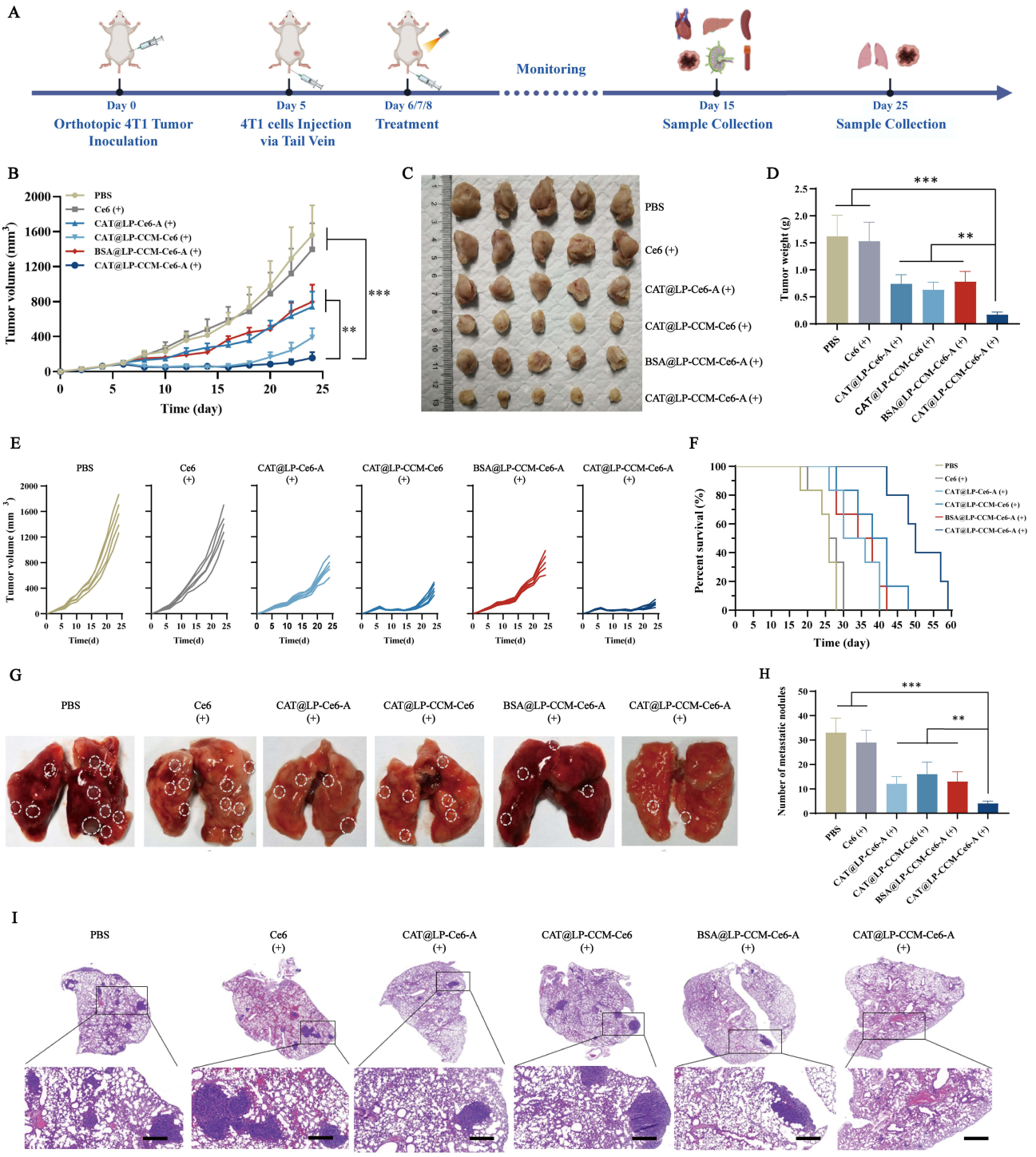

Figure 5 In vivo antitumor effect. (**A**) Schematic illustration of the treatment program. This was created with BioRender. (**B**) Growth curves of primary tumor in mice (n = 5). (**C**) Visual comparison of tumors excised from the mice in each group (n = 5). (**D**) The tumor weight on day 24 received various treatments (n = 5). (**E**) Individual tumor growth after different treatments (n = 5). (**F**) The survival curves of mice in different treatment groups (n = 5). (**G**) Metastatic nodules in the lungs, the white circles denoted the metastatic nodules. (**H**) Numbers of lung metastatic nodules in each group (n = 5). (**I**) H&E staining of the excised lungs. (+) was the treatment plus 660nm laser. Scale bar = 200 μm. (+) refers to 660 nm laser irradiation. Data are expressed as mean ± SD. ***P*<0.01, *** *P*<0.001.

As shown in Figure 6F and G, a remarkable increase in the proportion of $CD8^+$ T cells (35.2 ± 5.1%) was observed in the tumor of mice exposed to CAT@LP-CCM-Ce6-A (with irradiation), which further contributed to the eradication of the tumor. The combined results suggested that CAT@LP-CCM-Ce6-A-based photodynamic immunotherapy elicited powerful antitumor

https://doi.org/10.2147/IJN.S508696

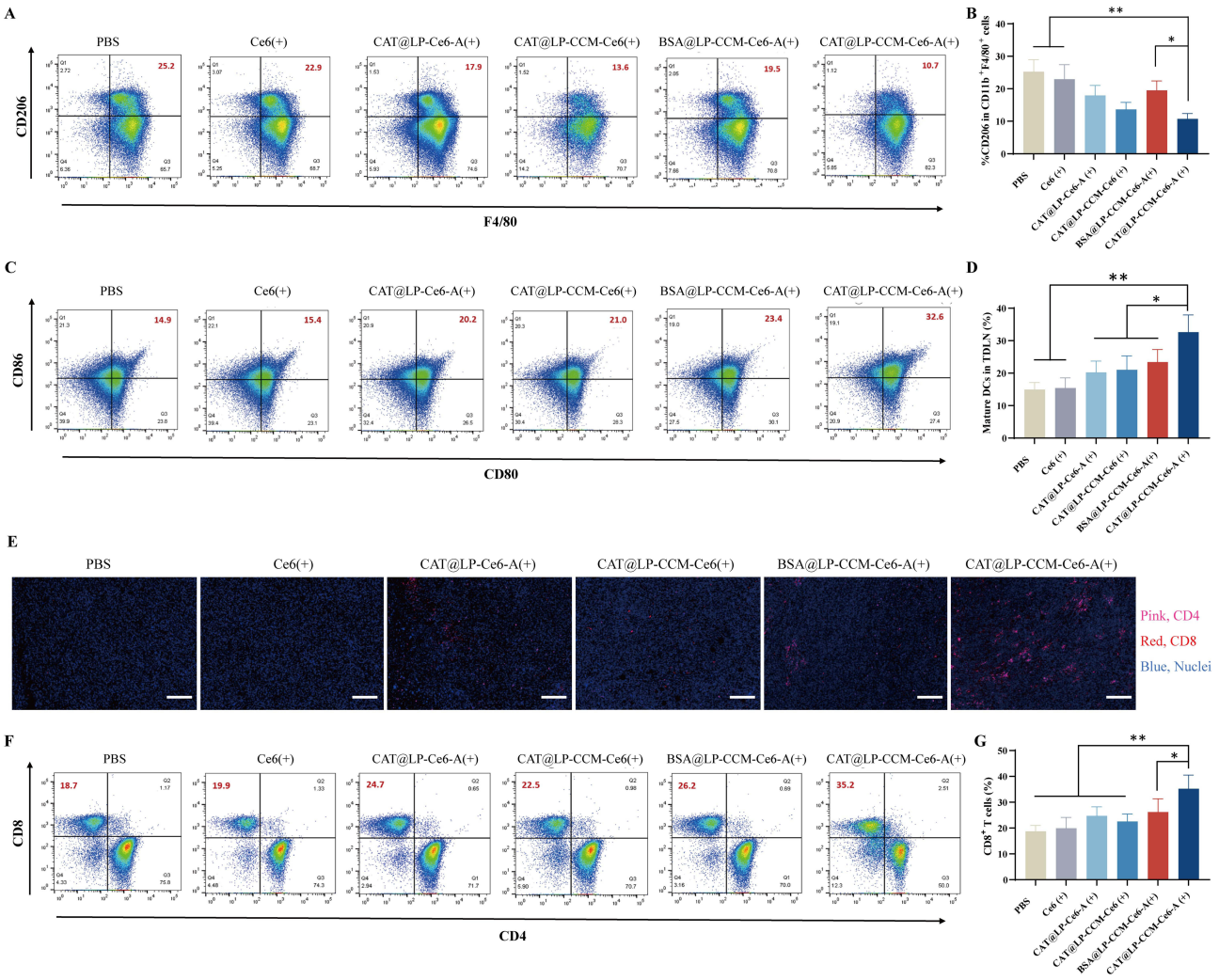

Figure 6 Enhanced antitumor immunity of CAT@LP-CCM-Ce6-A-based PDIT. (**A**) Flow cytometric analysis of M2-macrophages ($CD206^+$) in $F4/80^+$ cells in tumors, and (**B**) the column statistical data. (**C**) Flow cytometric analysis of the induction of DCs maturation in TDLNs, and (**D**) the column statistical data. (**E**) Immunofluorescence staining of $CD8^+$ T cells (red) and $CD4^+$ T cells (pink) in tumor tissues, scale bar = 200 μm. (**F**) Flow cytometric analysis of the infiltration of $CD8^+$ T lymphocytes in tumors after different treatments, and (**G**) the column statistical data. (+) refers to 660 nm laser irradiation. Scale bar = 200 μm. Data are expressed as mean ± SD (n=3). *P<0.05, **P<0.01.

immunity through the release of MPLA and immunogenic substances, enhancing DCs maturation and T lymphocyte activation, leading to the suppression of primary tumor and inhibition of lung metastasis.

The Safety Profile of CAT@LP-CCM-Ce6-A

The hemolysis assay is a direct method to examine the potential safety of the injectable formulations. Therefore, we first conducted the hemolysis test to determine the potential compatibility of CAT@LP-CCM-Ce6-A by measuring the lysis of red blood cells (Figure S3). Complete hemolysis was observed in red blood cells diluted with the water (positive control), while the tube of CAT@LP-CCM-Ce6-A was nearly transparent with the red blood cells sedimentation, indicating that CAT@LP-CCM-Ce6-A did not induce hemolysis and possessed ideal safety in circulation. To further investigate the in vivo safety properties of CAT@LP-CCM-Ce6-A, the weight of the tumor-bearing mice was monitored for 24 days. During the PDIT process, insignificant fluctuation of body weight was observed (Figure S4), indicating the potential biosafety of CAT@LP-CCM-Ce6-A. To further evaluate the safety profile of CAT@LP-CCM-Ce6-A, H&E staining of major organs including the heart, liver, spleen, and kidney was conducted to observe potential toxicity or side effects caused by CAT@LP-CCM-Ce6-A based PDIT. H&E staining analyses revealed no significant toxicity caused by

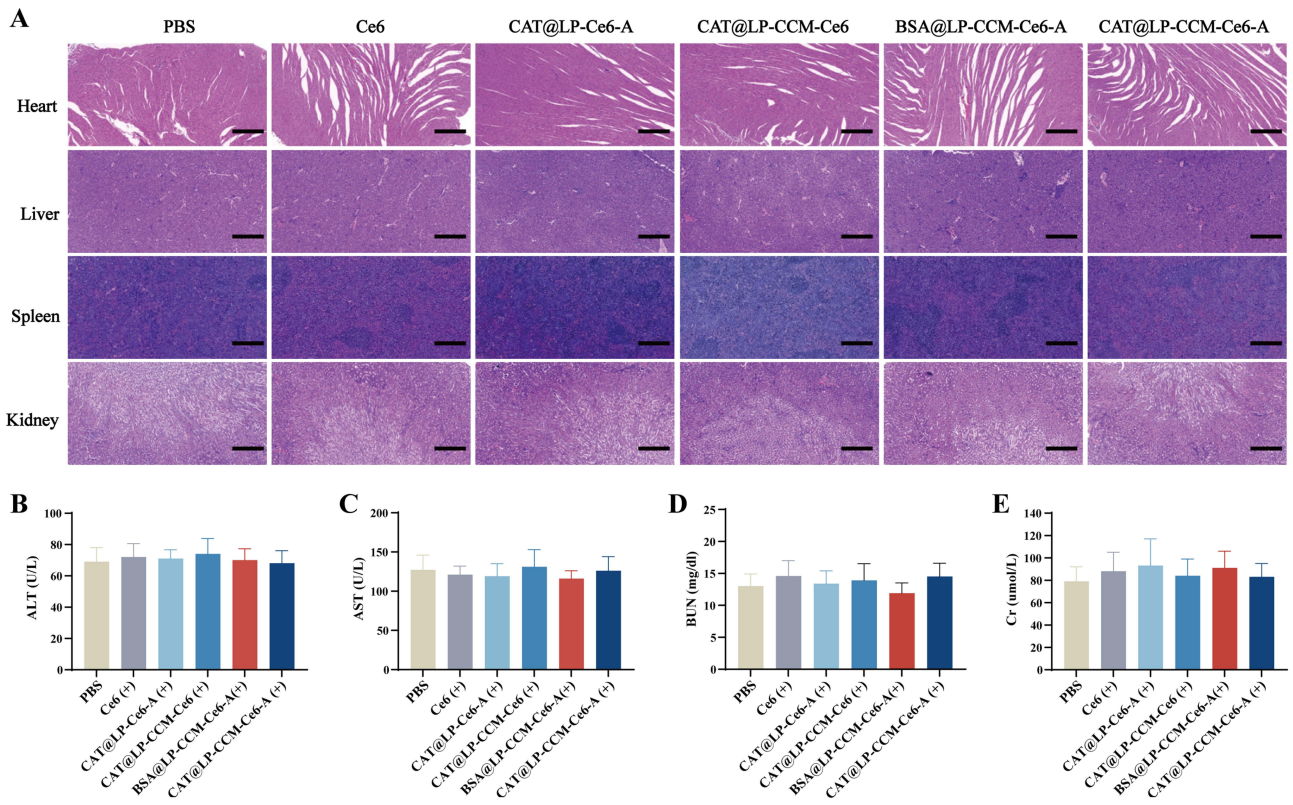

Figure 7 The in vivo safety properties of CAT@LP-CCM-Ce6-A. (**A**) H&E staining of major organs in mice treated with different formulations. Serum levels of (**B**) alanine aminotransferase (ALT), (**C**) aspartate aminotransferase (AST), (**D**) urea nitrogen (BUN) and (**E**) creatinine (Cr) in tumor-bearing mice after treatment (n=3). Scale bar = 200 μm. Data are expressed as mean ± SD (n=3).

CAT@LP-CCM-Ce6-A treatment in TNBC lung metastasis mouse models (Figure 7A). Additionally, we analyzed the relative levels of ALT and AST to reflect liver functions, and BUN and Cr to reflect renal functions (Figure 7B–E). Briefly, the serum levels of ALT, AST, BUN, and Cr demonstrated that CAT@LP-CCM-Ce6-A was safe with all these indexes within normal reference ranges.

Conclusion

In this study, we have successfully designed a biomimetic self-oxygenated immunoliposome containing CAT, photosensitizer Ce6, and immune adjuvant MPLA. CAT@LP-CCM-Ce6-A exhibited high affinity and targeting ability toward tumors, as well as robust oxygen-producing capabilities. CAT released from CAT@LP-CCM-Ce6-A catalyzes endogenous H_2O_2 in tumors to produce oxygen to improve hypoxia. Under laser irradiation, CAT@LP-CCM-Ce6-A produced a substantial quantity of $^1O_2$, killing tumor cells directly and releasing immunogenic substances to induce the DCs maturation. Simultaneously, immune adjuvant MPLA released from CAT@LP-CCM-Ce6-A further amplified the intensity of the immune response, thereby boosting antitumor immunity and further suppressing TNBC lung metastasis.

In summary, CAT@LP-CCM-Ce6-A represents an innovative strategy for self-oxygenated PDIT against metastatic tumors.

Data Sharing Statement

The datasets generated during and/or analyzed during the current study are available from the corresponding author upon reasonable request.

Consent for Publication

All authors declare that they have read the final version of the manuscript and have agreed to its submission for publication.

https://doi.org/10.2147/IJN.S508696

Funding

This research was supported by the Natural Science Foundation of Hunan Province, China (grant number 2025JJ80100, 2024JJ5480)and the Natural Science Foundation of Changsha, Hunan Province, China (kq2403089).

Disclosure

The authors report no conflicts of interest in this work.

References

1. Valastyan S, Weinberg RA. Tumor metastasis: molecular insights and evolving paradigms. *Cell*. 2011;147(2):275–292. doi:10.1016/j.cell.2011.09.024
2. Sang W, Zhang Z, Dai Y, Chen X. Recent advances in nanomaterial-based synergistic combination cancer immunotherapy. *Chem Soc Rev*. 2019;48(14):3771–3810. doi:10.1039/c8cs00896e
3. Chen Z, Liu L, Liang R, et al. Bioinspired Hybrid Protein Oxygen Nanocarrier Amplified Photodynamic Therapy for Eliciting Anti-tumor Immunity and Abscopal Effect. *ACS Nano*. 2018;12(8):8633–8645. doi:10.1021/acsnano.8b04371
4. Zhang N, Zhao F, Zou Q, Li Y, Ma G, Yan X. Multitriggered Tumor-Responsive Drug Delivery Vehicles Based on Protein and Polypeptide Coassembly for Enhanced Photodynamic Tumor Ablation. *Small*. 2016;12(43):5936–5943. doi:10.1002/smll.201602339
5. Thong PS, Ong KW, Goh NS, et al. Photodynamic-therapy-activated immune response against distant untreated tumours in recurrent angiosarcoma. *Lancet Oncol*. 2007;8(10):950–952. doi:10.1016/s1470-2045(07)70318-2
6. Alzeibak R, Mishchenko TA, Shilyagina NY, Balalaeva IV, Vedunova MV, Krysko DV. Targeting immunogenic cancer cell death by photodynamic therapy: past, present and future. *J Immunother Cancer*. 2021;9(1):1. doi:10.1136/jitc-2020-001926
7. Ji B, Wei M, Yang B. Recent advances in nanomedicines for photodynamic therapy (PDT)-driven cancer immunotherapy. *Theranostics*. 2022;12(1):434–458. doi:10.7150/thno.67300
8. Donohoe C, Senge MO, Arnaut LG, Gomes-da-Silva LC. Cell death in photodynamic therapy: from oxidative stress to anti-tumor immunity. *Biochim Biophys Acta Rev Cancer*. 2019;1872(2):188308. doi:10.1016/j.bbcan.2019.07.003
9. Meier P, Legrand AJ, Adam D, Silke J. Immunogenic cell death in cancer: targeting necroptosis to induce antitumour immunity. *Nat Rev Cancer*. 2024;24(5):299–315. doi:10.1038/s41568-024-00674-x
10. Yu X, Gao D, Gao L, et al. Inhibiting Metastasis and Preventing Tumor Relapse by Triggering Host Immunity with Tumor-Targeted Photodynamic Therapy Using Photosensitizer-Loaded Functional Nanographenes. *ACS Nano*. 2017;11(10):10147–10158. doi:10.1021/acsnano.7b04736
11. Liang R, Liu L, He H, et al. Oxygen-boosted immunogenic photodynamic therapy with gold nanocages@manganese dioxide to inhibit tumor growth and metastases. *Biomaterials*. 2018;177:149–160. doi:10.1016/j.biomaterials.2018.05.051
12. Kleinovink JW, van Driel PB, Snoeks TJ, et al. Combination of Photodynamic Therapy and Specific Immunotherapy Efficiently Eradicates Established Tumors. *Clin Cancer Res*. 2016;22(6):1459–1468. doi:10.1158/1078-0432.Ccr-15-0515
13. Zou MZ, Liu WL, Chen HS, et al. Advances in nanomaterials for treatment of hypoxic tumor. *Natl Sci Rev*. 2021;8(2):nwaa160. doi:10.1093/nsr/nwaa160
14. Xx X, Sy C, Nb Y, et al. Research progress on tumor hypoxia-associative nanomedicine. *J Control Release*. 2022;350:829–840. doi:10.1016/j.jconrel.2022.09.003
15. Semenza GL. Targeting intratumoral hypoxia to enhance anti-tumor immunity. *Semin Cancer Biol*. 2023;96:5–10. doi:10.1016/j.semcancer.2023.09.002
16. Kopecka J, Salaroglio IC, Perez-Ruiz E, et al. Hypoxia as a driver of resistance to immunotherapy. *Drug Resist Updat*. 2021;59:100787. doi:10.1016/j.drup.2021.100787
17. Liao C, Liu X, Zhang C, Zhang Q. Tumor hypoxia: from basic knowledge to therapeutic implications. *Semin Cancer Biol*. 2023;88:172–186. doi:10.1016/j.semcancer.2022.12.011
18. Jing X, Yang F, Shao C, et al. Role of hypoxia in cancer therapy by regulating the tumor microenvironment. *mol Cancer*. 2019;18(1):157. doi:10.1186/s12943-019-1089-9
19. Yang N, Xiao W, Song X, Wang W, Dong X. Recent Advances in Tumor Microenvironment Hydrogen Peroxide-Responsive Materials for Cancer Photodynamic Therapy. *Nanomicro Lett*. 2020;12(1):15. doi:10.1007/s40820-019-0347-0
20. Wu Q, You L, Nepovimova E, et al. Hypoxia-inducible factors: master regulators of hypoxic tumor immune escape. *J Hematol Oncol*. 2022;15(1):77. doi:10.1186/s13045-022-01292-6
21. Bai R, Li Y, Jian L, Yang Y, Zhao L, Wei M. The hypoxia-driven crosstalk between tumor and tumor-associated macrophages: mechanisms and clinical treatment strategies. *mol Cancer*. 2022;21(1):177. doi:10.1186/s12943-022-01645-2
22. Cassetta L, Pollard JW. A timeline of tumour-associated macrophage biology. *Nat Rev Cancer*. 2023;23(4):238–257. doi:10.1038/s41568-022-00547-1
23. Kleinovink JW, Fransen MF, Löwik CW, Ossendorp F. Photodynamic-Immune Checkpoint Therapy Eradicates Local and Distant Tumors by CD8 (+) T Cells. *Cancer Immunol Res*. 2017;5(10):832–838. doi:10.1158/2326-6066.Cir-17-0055
24. Song W, Kuang J, Li CX, et al. Enhanced Immunotherapy Based on Photodynamic Therapy for Both Primary and Lung Metastasis Tumor Eradication. *ACS Nano*. 2018;12(2):1978–1989. doi:10.1021/acsnano.7b09112
25. Shi C, Li M, Zhang Z, et al. Catalase-based liposomal for reversing immunosuppressive tumor microenvironment and enhanced cancer chemo-photodynamic therapy. *Biomaterials*. 2020;233:119755. doi:10.1016/j.biomaterials.2020.119755
26. Gnanasekar S, Kasi G, He X, Zhang K, Xu L, Kang ET. Recent advances in engineered polymeric materials for efficient photodynamic inactivation of bacterial pathogens. *Bioact Mater*. 2023;21:157–174. doi:10.1016/j.bioactmat.2022.08.011
27. Wang C, Chen S, Yu F, et al. Dual-Channel Theranostic System for Quantitative Self-Indication and Low-Temperature Synergistic Therapy of Cancer. *Small*. 2021;17(10):e2007953. doi:10.1002/smll.202007953

28. Pucci C, De Pasquale D, Degl'Innocenti A, et al. Chlorin e6-Loaded Nanostructured Lipid Carriers Targeted by Angiopep-2: advancing Photodynamic Therapy in Glioblastoma. *Adv Healthc Mater*. 2025;14(2):e2402823. doi:10.1002/adhm.202402823
29. Mata-Haro V, Cekic C, Martin M, Chilton PM, Casella CR, Mitchell TC. The vaccine adjuvant monophosphoryl lipid A as a TRIF-biased agonist of TLR4. *Science*. 2007;316(5831):1628–1632. doi:10.1126/science.1138963
30. Cheng H, Jiang XY, Zheng RR, et al. A biomimetic cascade nanoreactor for tumor targeted starvation therapy-amplified chemotherapy. *Biomaterials*. 2019;195:75–85. doi:10.1016/j.biomaterials.2019.01.003
31. Chen Z, Zhao P, Luo Z, et al. Cancer Cell Membrane-Biomimetic Nanoparticles for Homologous-Targeting Dual-Modal Imaging and Photothermal Therapy. *ACS Nano*. 2016;10(11):10049–10057. doi:10.1021/acsnano.6b04695
32. Chen B, Dai W, He B, et al. Current Multistage Drug Delivery Systems Based on the Tumor Microenvironment. *Theranostics*. 2017;7(3):538–558. doi:10.7150/thno.16684
33. Wu M-Y, Wu Z-J, Wang J-L, et al. Single Molecule for Trifecta PDT: tailor-Made Three-Organelle-Targeting Type I Photosensitizer for Cancer Cell-Selective Photodynamic Therapy under Hypoxia. *ACS Mater Lett*. 2024;6(10):4533–4544. doi:10.1021/acsmaterialslett.4c01214
34. Wang Y, Li F, Wei S, et al. Puerarin-Loaded Liposomes Co-Modified by Ischemic Myocardium-Targeting Peptide and Triphenylphosphonium Cations Ameliorate Myocardial Ischemia-Reperfusion Injury. *Int J Nanomed*. 2024;19:7997–8014. doi:10.2147/ijn.S468394
35. Gao M, Liang C, Song X, et al. Erythrocyte-Membrane-Enveloped Perfluorocarbon as Nanoscale Artificial Red Blood Cells to Relieve Tumor Hypoxia and Enhance Cancer Radiotherapy. *Adv Mater*. 2017;29(35):1429. doi:10.1002/adma.201701429
36. Zhang Y, Jia R, Wang X, et al. Targeted Delivery of Catalase and Photosensitizer Ce6 by a Tumor-Specific Aptamer Is Effective against Bladder Cancer In Vivo. *Mol Pharm*. 2024;21(4):1705–1718. doi:10.1021/acs.molpharmaceut.3c01047
37. Chen Q, Chen J, Yang Z, et al. Nanoparticle-Enhanced Radiotherapy to Trigger Robust Cancer Immunotherapy. *Adv Mater*. 2019;31(10):1802228. doi:10.1002/adma.201802228
38. Feng L, Cheng L, Dong Z, et al. Theranostic Liposomes with Hypoxia-Activated Prodrug to Effectively Destruct Hypoxic Tumors Post-Photodynamic Therapy. *ACS Nano*. 2017;11(1):927–937. doi:10.1021/acsnano.6b07525
39. He C, Duan X, Guo N, et al. Core-shell nanoscale coordination polymers combine chemotherapy and photodynamic therapy to potentiate checkpoint blockade cancer immunotherapy. *Nat Commun*. 2016;7(1):12499. doi:10.1038/ncomms12499
40. Li Z, Lai X, Fu S, et al. Immunogenic Cell Death Activates the Tumor Immune Microenvironment to Boost the Immunotherapy Efficiency. *Adv Sci*. 2022;9(22):e2201734. doi:10.1002/advs.202201734
41. Yang W, Zhu G, Wang S, et al. In Situ Dendritic Cell Vaccine for Effective Cancer Immunotherapy. *Acs Nano*. 2019;13(3):3083–3094. doi:10.1021/acsnano.8b08346
42. Kim H, Niu L, Larson P, et al. Polymeric nanoparticles encapsulating novel TLR7/8 agonists as immunostimulatory adjuvants for enhanced cancer immunotherapy. *Biomaterials*. 2018;164:38–53. doi:10.1016/j.biomaterials.2018.02.034
43. Dang J, He H, Chen D, Yin L. Manipulating tumor hypoxia toward enhanced photodynamic therapy (PDT). *Biomater Sci*. 2017;5(8):1500–1511. doi:10.1039/c7bm00392g
44. Xiang X, Wang J, Lu D, Xu X. Targeting tumor-associated macrophages to synergize tumor immunotherapy. *Signal Transduct Target Ther*. 2021;6(1):75. doi:10.1038/s41392-021-00484-9
45. Mao X, Xu J, Wang W, et al. Crosstalk between cancer-associated fibroblasts and immune cells in the tumor microenvironment: new findings and future perspectives. *mol Cancer*. 2021;20(1):131. doi:10.1186/s12943-021-01428-1